LAWRENCE
LIVERMORE
NATIONAL
LABORATORY

LLNL-JRNL-401832

Intercomparison of model simulations of mixed-phase clouds observed during the ARM Mixed-Phase Arctic Cloud Experiment. Part II: Multi-layered cloud

H. Morrison, R. B. McCoy, S. A. Klein, S. Xie, Y. Luo, A. Avramov, M. Chen, J. Cole, M. Falk, M. Foster, A. Del Genio, J. Harrington, C. Hoose, M. Khairoutdinov, V. Larson, X. Liu, G. McFarquhar, M. Poellot, B. Shipway, M. Shupe, Y. Sud, D. Turner, D. Veron, G. Walker, Z. Wang, A. Wolf, K.-M. Xu, F. Yang, G. Zhang

February 29, 2008

Quarterly Journal of the Royal Meteorological Society

Disclaimer

Intercomparison of model simulations of mixed-phase clouds observed during the ARM Mixed-Phase Arctic Cloud Experiment, Part II: Multi-layered cloud

Hugh Morrison[1*], Renata McCoy[2], Stephen Klein[2], Shaocheng Xie[2], Yali Luo[7], Alexander Avramov[3], Mingxuan Chen[4], Jason Cole[10], Michael Falk[17], Michael Foster[16], Anthony Del Genio[13], Jerry Harrington[3], Corinna Hoose[9], Marat Khairoutdinov[5], Vincent Larson[17], Xiaohong Liu[6], Greg McFarquhar[18], Michael Poellot[22], Ben Shipway[15], Matthew Shupe[19], Yogesh Sud[12], David Turner[20], Dana Veron[14], Gregory Walker[12], Zhien Wang[21], Audrey Wolf[13], Kuan-Man Xu[8], Fanglin Yang[11], and Gong Zhang[18]

Draft, February 27, 2008, to be submitted to *Q. J. Roy. Meteor. Soc.*

[*]Corresponding author address: Hugh Morrison, National Center for Atmospheric Research, 3450 Mitchell Lane, Boulder, CO, 80307

[1]National Center for Atmospheric Research, Boulder, CO, USA
[2]Energy and Environment Directorate, Lawrence Livermore National Laboratory, Livermore, CA, USA
[3]The Pennsylvania State University, University Park, PA, USA
[4]Colorado State University, Fort Collins, CO, USA
[5]State University of New York at Stony Brook, Stony Brook, NY, USA
[6]Pacific Northwest National Laboratory, Richland, WA, USA
[7]State Key Laboratory of Severe Weather, Chinese Academy of Meterological Sciences, Beijing, China
[8]NASA Langley Research Center, Hampton, VA, USA
[9]ETH Zurich, Institute for Atmospheric and Climate Science, Zurich, Switzerland
[10]University of British Columbia, Vancouver, BC, Canada
[11]National Centers for Environmental Prediction, Camp Springs, MD, USA
[12]NASA Goddard Space Flight Center, Greenbelt, MD, USA
[13]NASA Goddard Institute for Space Studies, New York, NY, USA
[14]University of Delaware, Newark, DE, USA
[15]Met Office, Exeter, United Kingdom
[16]Rutgers University, New Brunswick, NJ, USA
[17]University of Wisconsin – Milwaukee, Milwaukee, WI, USA

[18]University of Illinois, Urbana, IL, USA
[19]Cooperative Institute for Research in Environmental Sciences, University of Colorado/NOAA, Boulder, CO, USA
[20]University of Wisconsin - Madison, Madison, WI, USA
[21]University of Wyoming, Laramie, WY, USA
[22]University of North Dakota, Grand Forks, ND, USA

Abstract.

Results are presented from an intercomparison of single-column and cloud-resolving model simulations of a deep, multi-layered, mixed-phase cloud system observed during the ARM Mixed-Phase Arctic Cloud Experiment. This cloud system was associated with strong surface turbulent sensible and latent heat fluxes as cold air flowed over the open Arctic Ocean, combined with a low pressure system that supplied moisture at mid-level. The simulations, performed by 13 single-column and 4 cloud-resolving models, generally overestimate the liquid water path and strongly underestimate the ice water path, although there is a large spread among the models. This finding is in contrast with results for the single-layer, low-level mixed-phase stratocumulus case in Part I of this study, as well as previous studies of shallow mixed-phase Arctic clouds, that showed an underprediction of liquid water path. The overestimate of liquid water path and underestimate of ice water path occur primarily when deeper mixed-phase clouds extending into the mid-troposphere were observed. These results suggest important differences in the ability of models to simulate Arctic mixed-phase clouds that are deep and multi-layered versus shallow and single-layered. In general, models with a more sophisticated, two-moment treatment of the cloud microphysics produce a somewhat smaller liquid water path that is closer to observations. The cloud-resolving models tend to produce a larger cloud fraction than the single-column models. The liquid water path and especially the cloud fraction have a large impact on the cloud radiative forcing at the surface, which is dominated by the longwave flux for this case.

1. Introduction

Recent field experiments have highlighted the common occurrence of mixed-phase stratiform clouds throughout the year in the Arctic, especially during the transition seasons (e.g., Curry et al. 2000; Intrieri et al. 2002; Shupe et al. 2006; Verlinde et al. 2007). The persistence of mixed-phase clouds for extended periods of time at temperatures significantly below freezing has important consequences for the cloud radiative forcing at the surface and hence surface energy budget and sea ice mass balance, since these clouds tend to be optically thicker than clouds composed solely of ice (Sun and Shine 1994; Shupe and Intrieri 2004; Zuidema et al. 2005; Turner 2005).

Observations during the 1997-98 Surface Heat Budget of the Arctic Ocean experiment (SHEBA) showed that when mixed-phase clouds were present, they consisted of a single liquid layer slightly more than half of the time. However, deeper mixed-phase cloud systems containing multiple, distinct layers of liquid were also common (Shupe et al. 2006). These clouds may be similar to the multilayered, liquid-phase stratus that commonly occur in the Arctic during summer (e.g., Jayaweera and Ohtake 1973; Herman and Goody 1976; Tsay and Jayaweera 1984; Curry 1986; Curry et al. 1998). Several theories have attempted to explain this multiple layering (see the review in Curry et al. 1996 for details), but it is unclear which mechanism(s) may be most important. Multi-layer, mixed-phase clouds have also been observed in mid-latitudes (Fleishauer et al. 2002).

Few studies have focused on multi-layered, mixed-phase stratus despite their fairly common occurrence in the Arctic. Presumably, some of the mechanisms proposed to explain multilayered liquid clouds may also pertain to multilayered mixed-phase

clouds. However, the presence of ice complicates the picture. Ice crystals falling from upper layers can seed the lower layers, depleting liquid water through riming and the Bergeron-Findeisen process (preferential vapor depositional growth of ice at the expense of liquid due to the lower ice saturation vapor pressure). The sublimation of crystals falling into dry layers may also impact the local static stability. Under some conditions this can result in a decoupling of well-mixed layers from each other and between the lower layer and the surface, and can promote the formation of a secondary, lower-level cloud layer (Harrington et al. 1999).

To further our understanding of Arctic mixed-phase cloud processes and provide a detailed observational dataset for model evaluation, the Mixed-Phase Arctic Cloud Experiment (M-PACE; Verlinde et al. 2007) was recently conducted over northern Alaska and the adjacent Arctic Ocean during September-October, 2004. M-PACE consisted of a suite of in-situ and remotely-based instruments that gathered measurements of mixed-phase cloud microphysics, dynamics, radiation, and aerosol. These data has been used to evaluate and constrain several models in previous studies (Xie et al. 2006; Luo et al. 2008a,b; Prenni et al. 2007; Fridlind et al. 2007; Morrison et al. 2008; Xie et al. 2008; Liu et al. 2007)

This study compares simulations of mixed-phase clouds observed during M-PACE using several single-column, cloud-resolving, and large-eddy models. Part I of the study (Klein et al. 2008; hereafter Part I) examines model results for a single-layer mixed-phase cloud. The current paper, part two of this study, describes results for a deeper, multi-layered, mixed-phase cloud system. The goals here are to document the current state of simulations for this type of cloud system, to understand sources of

differences in the simulations, and to spur improvements in their representation in climate and weather models. Herein, the approach is taken to subject each model to the same initial condition and advective tendencies of the large-scale circulation as was done in previous model intercomparison studies performed under the auspices of the GEWEX Cloud Systems Study (GCSS) project (Randall et al. 2003, GEWEX is the Global Energy and Water Experiment). This intercomparison is the first such activity of the GCSS Polar Cloud Working Group and was performed jointly with the ARM Cloud Modeling Working Group.

The paper is organized as follows. Section 2 gives a case description. Section 3 provides an overview of the instrumentation and observations. Section 4 describes the experimental design. Brief descriptions of the participating models are provided in section 5. Section 6 discusses the baseline model results. Sensitivity tests are described in section 7. Finally, summary and conclusions are given in section 8.

2. Case description

M-PACE was conducted from September 27 through October 22 over the North Slope of Alaska and adjacent Arctic Ocean (Verlinde et al. 2007). M-PACE sought to collect a comprehensive dataset to investigate physical processes in mixed-phase clouds using two research aircraft and a host of ground-based instrumentation. The M-PACE domain consisted of the region bounded by four surface sites: Barrow, Atqasuk, Toolik Lake, and Oliktok Point (Fig. 1).

In this study, we focus on the multi-layered, mixed-phase cloud that was observed during Oct. 5-8, 2004. This cloud system was associated with a rather complex synoptic-

scale flow field. An anticyclone to the north of Alaska over the ice-covered central Arctic Ocean brought persistent flow from the east-northeast at low levels with considerable fetch over the open water of the Beaufort Sea. The flow of cold air from the pack ice and over open water drove the formation of boundary layer clouds that advected over the North Slope of Alaska, similar to the low-level, single-layer case described in Part I. However, a small, mid-level low pressure system drifted into the M-PACE domain from the east that also promoted considerable moistening and cloudiness at mid-levels, in contrast to the case in Part I. The time evolution of cloudiness at Barrow (Fig. 2) is illustrated by the cloud fraction derived from the Active Remotely-Sensed Cloud Locations (ARSCL) algorithm (Clothiaux et al. 2000).

The deep, multi-layered cloud system on Oct. 6 and 7 consisted of a number of distinct liquid layers with ice crystals falling between the liquid layers as indicated by aircraft measurements (Fig. 3). This complex, multi-layered cloud structure was also captured by ground-based remote sensing, i.e., the Arctic High Spectral Resolution Lidar (Eloranta 2005). The ice particles that extended through the depth of the cloud system reached the surface in the form of light snow showers. Interestingly, the liquid layers appeared to be associated with well-mixed layers that were decoupled from each other (indicated by the profile of liquid water potential temperature seen in Figure 3). Elevated well-mixed layers associated with mixed-phase clouds have been previously observed in the Arctic (e.g., Pinto 1998) as well as in mid-latitudes (Fleishauer et al. 2002).

3. Observations.

The University of North Dakota Citation aircraft, which provided detailed in-situ microphysical data used in this study, was based at Oliktok Point and flew a number of spirals over Barrow and Oliktok Point as well as ramped ascents and descents between the two sites (see Fig. 5 in Verlinde et al. 2007 for an example of a typical flight pattern). Several instruments were deployed on the Citation that provided detailed cloud microphysical measurements (McFarquhar et al. 2007a). These probes measured the size distribution of particles with diameters between 3 μm and 40 mm, as well as the total condensate and liquid water contents separately. Cloud phase was determined to be either liquid only, ice only, or mixed-phase from an algorithm that considered the output of an icing detector, visual inspection of particle images, and the shape of the particle size distribution (see Figure 2 in McFarquhar et al. 2007a). The phase classification was made for each 30 second flight segment that was determined to contained cloud. A 30-second segment corresponds approximately to 2.5 kilometers of horizontal distance. There were three flights (on Oct. 5, 6, 8) during this case, with a total of about 7.7 flight hours; about 5 flight hours were in clouds and/or precipitation. Most samples were below 2 km, with no samples taken below 400 m. In addition to cloud phase, derived bulk parameters include liquid and ice water contents as well as particle number concentration and effective radius determined separately for liquid and ice. For measurement in ice-phase clouds, derived parameters only include contributions from particles with maximum dimension greater than 53 μm because the shattering of large crystals on protruding tips of probes (McFarquhar et al. 2007b) may artificially enhance concentrations of small particles. In mixed-phase clouds, particles smaller than 53 μm are assumed to be supercooled water droplets. Ice effective radius is calculated using the

definition of Fu (1996). Rough estimates of uncertainty are ± 15% for the bulk liquid parameters and a factor of 2 for the bulk ice parameters. For further details of the methods used to determine these parameters see McFarquhar et al. (2007a).

Ground-based instruments were deployed at the NSA surface sites. These instruments included two-channel microwave radiometer, lidar, and millimeter cloud radar to determine liquid water path (Turner et al. 2007, hereafter TURNER; Wang 2007, hereafter WANG), profiles of ice water content (Shupe et al. 2006, hereafter SHUPE-TURNER), and cloud occurrence, boundaries, and phase (Wang and Sassen 2001; Shupe 2007; Wang 2007). Liquid water path is available from Oliktok Point, Atqasuk, and Barrow, while the other cloud property retrievals are available only for Barrow. A rough estimate of the uncertainty is a factor of 2 for the bulk ice parameters and ± 15% for the bulk liquid parameters, similar to the aircraft observations. Note that there is additional uncertainty because of issues related to the representativeness of the surface sites to the domain as a whole.

Profiles of temperature, water vapor mixing ratio, and horizontal winds were obtained from sounding balloons launched every 6 hours from the four surface sites bounding the M-PACE domain. Surface measurements were only available at Barrow, Atqasuk, and Oliktok Point. Surface observations used here to compare with the models include upwelling and downwelling radiative fluxes and precipitation rate.

4. Experimental design

The model specifications for this intercomparison are similar to previous ARM intercomparison studies for the ARM Southern Great Plains site (e.g., Ghan et al. 2000;

Xie et al. 2005; Xu et al. 2005), with participation from both single-column models (representing a single grid cell of a general circulation or weather prediction model), and cloud-resolving models. The fairly large domain in the vertical dimension precluded the participation of higher-resolution large-eddy models, although these models did participate in Part I. The simulation period is from 1400 UTC October 5 to 1400 UTC October 8.

Initial conditions and large-scale forcings used by all participating models are derived from the ARM variational analysis for M-PACE (Xie et al. 2006). Initial profiles are based on the observed areal-averages of temperature, water vapor mixing ratio, and horizontal wind velocity for the M-PACE region at 25 mb increments in the vertical. Above 215 mb, a standard Arctic profile is applied to the initial fields.

The primary forcing terms in the SCM/CRM governing equations are the large-scale advective tendencies of temperature and water vapor mixing ratio. The large-scale forcings are based on the variational analysis calculated over the 4-sided 240 x 100 km grid shown in Fig. 1. Large-scale forcings from the variational analysis are calculated between 1015 and 90 mb. Forcings above 90 mb are obtained by interpolation, assuming tendencies of zero at a height of 20 km. The large-scale advective forcings of temperature, $\overline{T}$, and water vapor mixing ratio, $\overline{q}$, are specified using the total (sometimes called "revealed") advective forcing, defined on isobaric surfaces as

$$\left(\frac{\partial \overline{T}}{\partial t}\right)_{L.S} \equiv -\vec{v}\cdot\nabla\overline{T} - \omega\frac{\partial \overline{T}}{\partial p} + \frac{\omega}{c_p}\alpha \qquad (1)$$

and

$$\left(\frac{\partial \overline{q}}{\partial t}\right)_{L.S} \equiv -\vec{v}\cdot\nabla\overline{q} - \omega\frac{\partial \overline{q}}{\partial p} \qquad (2)$$

where p is pressure, ω is the large-scale vertical pressure velocity, c_p is the specific heat of air at constant pressure, $\vec{v}$ is the large-scale 2D wind vector, ∇ is the horizontal del operator, and α is the specific volume of air (the inverse of air density). The advective forcings derived for the period are shown in Fig. 4. The large-scale advection of hydrometeors is neglected since these terms were not calculated in the analysis. The profile of large-scale horizontal wind is also derived from the variational analysis. The models were asked to maintain this large-scale wind profile in whatever way they saw fit (most models used nudging).

The lower surface is treated as land (except for the small fraction of the domain seen in Fig. 1 over ocean). Although there is some uncertainty given that the lower part of the cloud system advected from the open ocean, where surface fluxes were presumably larger than over land, we chose this model domain for consistency with the large-scale forcing from the variational analysis. Time-varying values of surface turbulent latent and sensible heat fluxes and surface temperature (needed for radiation calculations) are specified from the analysis. The time-averaged (between 000 UTC Oct. 6 and 1400 UTC Oct. 8) latent and sensible turbulent surface heat fluxes are 18 and 2 W m^{-2} respectively, while the surface skin temperature is -1.6^{o} C. Broadband visible albedo is specified at 0.85, corresponding with the snow-covered land surface.

Although there was day-to-day variability in the aerosol characteristics as indicated by measurements at the NOAA/ESRL Global Monitoring Division observatory located near Barrow (as well as inferred from variability in the aircraft droplet concentration measurements), pristine conditions and low aerosol loading was encountered during this case as well as the single-layer case in Part I. For simplicity, we

use the same aerosol and ice nuclei specifications as were used for the single-layer case (see Part I for details).

5. Model descriptions

a) Overview

Thirteen SCMs and four CRMs participated in the intercomparison for this case study. The SCMs include one operational weather prediction model (NCEP); five operational climate models (CCCMA, ECHAM, GFDL, GISS-LBL, SCAM3); and four models used primarily for research (ARCSCM, MCRAS, SCRIPPS, UWM). In addition, there are three models that were developed by modifying the base models to include a two-moment cloud microphysics scheme, i.e., a scheme that predicts both mixing ratios and number concentrations of the hydrometeor species (MCRASI, SCAM3-LIU, SCAM3-MG). The number of vertical levels is shown in Table 1, and ranges from 16 to 64.

Among the CRMs, two models are two-dimensional (UCLA-LARC, RAMS-CSU), and two are three-dimensional (SAM, METO). Horizontal resolution varies from 500 m (SAM, METO) to 1 km (RAMS-CSU) to 2 km (UCLA-LARC), with a domain size of about 60 to 250 km in the relevant horizontal dimension(s). The number of vertical levels in the baseline simulations ranges from 45 to 52 (see Table 1).

For model details, including references, see Tables 1 and 2 in Part 1. For brevity, this is not shown here[1].

[1] Note that the spatial resolution of some of the models differs here relative to that shown in Tables 1 and 2 in Part I; furthermore, not all of the models shown in Tables 1 and 2 in Part I participated here.

b) Description of the cloud microphysics

Since the microphysics may be a key in simulating mixed-phase clouds, we briefly describe its treatment here. A more complete description of the various microphysics schemes utilized by the models is given in Tables 1 and 2 of Part I. The parameterizations of cloud microphysics can be classified into three broad categories which span a wide range of complexity. However, all treatments of the microphysics in the models participating in this case use the bulk approach (prediction of bulk properties of the hydrometeor species such as mass mixing ratio, with an assumption of the underlying shape of the particle size distributions). There are no models participating in this case that use the bin approach (explicit prediction of the hydrometeor size distributions), although bin models did participate in Part I.

The simplest representation, which will be called "single-moment with T-dependent partitioning", employs a single prognostic variable for the mass of cloud condensate and uses a temperature-dependent function to partition the relative amount of liquid and ice. This approach is used by 3 SCMs (MCRAS, NCEP, SCAM3[2]) and 1 CRM (SAM).

The second class of cloud microphysics, "single-moment with independent liquid and ice", employs separate prognostic variables for the mass of condensate of cloud liquid and ice for which the relative amount of liquid and ice is not solely a function of temperature. 4 SCMs (CCCMA, GFDL, GISS, SCRIPPS, UWM) employ this class of microphysics. In these models, the relative amount of liquid and ice varies according to a number of considerations which typically include a temperature dependent partitioning of

[2] The SCAM3 microphysics includes separate prognostic variables for the cloud liquid and ice mixing ratios, although fraction of liquid and ice is repartitioned each time step according to temperature.

liquid and ice at cloud formation and subsequent conversion of liquid to ice through the Bergeron-Findeisen process, riming, and/or drop freezing. Hereafter, '1-M' will refer to single-moment schemes with either independent liquid and ice or T-dependent partitioning.

The third class of cloud microphysics, "double-moment", employs prognostic variables for both the mass of condensate as well as the number concentration of cloud and/or precipitation particles. 5 SCMs (ARCSCM, ECHAM, MCRASI, SCAM3-MG, SCAM3-LIU) and 3 CRMs (RAMS-CSU, UCLA-LARC, METO) employ this approach. An advantage over the previous two classes is that the prognostic representation of the number concentration potentially allows a more robust treatment of mean particle size as well as coupling with aerosol. All two-moment parameterizations in this study represent the number concentration of cloud (small) ice with a prognostic variable, while number concentrations of other species (cloud droplets, rain, snow, graupel, etc.) may or may not be represented as a prognostic variable (see Tables 1 and 2 in Part I). Hereafter, '2-M' will refer to models with two-moment microphysics schemes.

In general, only models with two-moment or bin microphysics represent the dependence of cloud properties on aerosols. However, one of the models with two-moment microphysics does not have an explicit dependence of cloud properties on aerosol (METO). Furthermore, not all models altered their default aerosol to that recommended in the intercomparison specifications. Thus, we do not focus on representation of cloud-aerosol interactions in this study. None of the models allowed two-way interaction between clouds and aerosols, except for RAMS-CSU, which allowed depletion of ice nuclei after nucleation and subsequent removal.

6. Baseline results

Simulations are compared for the period from 000 UTC Oct. 6 to 1400 UTC Oct. 8, which allows for 10 hours of model spin-up time. First, we compare results for the baseline simulations, and then we compare sensitivity tests with either higher vertical resolution or neglect of ice microphysics. The focus is on key cloud and thermodynamic properties that impact the cloud radiative forcing. Thus, we pay particular attention to the cloud liquid water path (which dominates the cloud ice water path in nearly all of the models), as well as the cloud fraction. The analysis is generally based on time-average results, although the modeled and observed cloud properties exhibit significant temporal variability over the period of interest as discussed below. This variability is in contrast with the single-layer case in Part I.

a) *Cloud morphology*

All of the models capture the general evolution of the cloud morphology during the period. An exception is that most of the models produce ice clouds between 300 and 500 mb during the latter part of Oct. 7 and first part of Oct. 8, which were not observed (see Fig. 2). These ice clouds appear to be associated with possibly spurious upper-level vertical motion and cold advection in the large-scale forcing data (see Fig. 4). Interestingly, nearly all of the models produce at least some of the multi-layered, mixed-phase cloud structure, with the exception of SAM. Here, the number of liquid layers occurring in the vertical is determined using a threshold cloud liquid water mixing ratio of 0.01 g kg-1, and a minimum separation distance of 50 m between the layers (note that

for the CRMs, the number of layers was calculated using horizontally-averaged data). This suggests that the overall occurrence of multi-layering in the simulations is more dependent on the large-scale atmospheric and surface forcing than details of the cloud microphysics or other aspects of the model physics. This finding is consistent with the model sensitivity study of Luo et al. (2008b), who found that the lower cloud layer was primarily driven by the surface turbulent heat fluxes, while the upper cloud layer was initially formed by large-scale advection and vertical motion and subsequently maintained by cloud-top radiative cooling. A few of the models here also produce persistent interior mixed-phase layers between the upper and lower layers (CCCMA, GISS); without further sensitivity studies, the mechanism(s) producing these layers is less clear.

Although nearly all of the models produce some multi-layering of cloud liquid water, the number of mixed-phase cloud layers (averaged over 000 UTC Oct. 6 to 1400 UTC Oct. 8) varies substantially among the simulations, from 1.00 in SAM to 3.10 in CCCMA. Thus, while the overall occurrence of multi-layering appears to be dependent mostly on the large-scale atmospheric and surface forcing, the actual number of layers depends on the details of the models. Surprisingly, the number of layers does not appear to be correlated with the vertical resolution. The observed time-averaged number of layers determined from ground-based retrievals at Barrow is 1.36, following the method of Wang and Sassen (2001). The presence of three or more layers occurred less than 10% of the time during this period (see Table 2 in Luo et al. 2008b). Thus, interior mixed-phase layers occurring between the upper and lower layers were rather infrequent.

However, we note that the number of layers may be somewhat underestimated due to retrieval uncertainty.

b. Cloud/hydrometeor fraction

Vertical profiles of the observed (ARSCL-derived) cloud/hydrometeor fraction and modeled cloud fraction, averaged over the period 000 UTC Oct. 6 to 1400 UTC Oct. 8, are shown in Figure 5. Note that the ARSCL observations do not include precipitation below the base of the lowest cloud layer, while they do include ice precipitation between mixed-phase cloud layers. All CRMs were asked to compute cloud fraction as the fraction of grid volumes with cloud droplet mixing ratios greater threshold of 0.01 g kg^{-1} or cloud ice mixing ratios greater than 0.0001 g kg^{-1}. Thus, individual grid cells have a cloud fraction of either 0 or 1 depending on the presence of cloud condensate exceeding these threshold values. The domain-average cloud fraction at a given level is then calculated by averaging the cloud fraction of each grid cell of the CRM at that level. For SCMs, cloud fraction is an inherent property of the model meant to represent the horizontal fraction of a grid-cell that is saturated and contains cloud water or ice.

Compared to the observations, all of the models produce too much cloud above 400 mb. This is related to the spurious production of ice clouds on Oct. 7 and 8 described previously. The median cloud fraction of the CRMs is larger (by about 10 – 30%) compared to the median of the SCMs. However, it is important to note that there is a large spread among both the CRMs and SCMs, indicated by the range and inner 50% of the model values shown in Figs. 5a. Furthermore, there may be some sensitivity to the condensate thresholds used here to define a “cloud” in the CRMs. Nonetheless,

differences in cloud fraction between the SCMs and CRMs appear to be significant and have an impact on the surface radiative fluxes as described later in this section.

The hydrometeor fraction (cloud and precipitation) is similarly larger for the CRMs than the SCMs, although the median hydrometeor fraction of the CRMs is larger than the ARSCL-derived observations (not shown). The hydrometeor fraction has less relevance to the cloud radiative forcing in models because they typically neglect the radiative impact of precipitation particles.

c) *Liquid and ice water contents*

Although all of the models produce a mostly overcast, precipitating mixed-phase clouds system, substantial differences exist in the predicted phase partitioning and cloud water and ice amounts. There is a large spread among the modeled cloud liquid water content (LWC) profiles averaged between 000 UTC Oct. 6 and 1400 UTC Oct. 14, indicated by the range and inner 50% model values in Fig. 6a. Here the LWC is an in-cloud value, found by dividing the reported grid-mean value by the cloud fraction (since the contribution of rain is small relative to cloud droplets in terms of the total liquid water content in all models, it is neglected). The median values for the CRMs are smaller than the median for the SCMs. However, the cloud fraction produced by the SCMs tends to be smaller than that of the CRMs; thus, the SCM and CRM median liquid water paths are similar as described in section 6e. Models with one-moment microphysics schemes tend to produce larger liquid water content, especially below 850 mb, relative to models with two-moment schemes (not shown). Aircraft observations are also shown in Fig. 6b. These values are in-cloud averages over the three flights that took place during the period (Oct.

5, 6, 8). There is significant variability within flights and especially between the flights, as indicated by the large standard deviation. The aircraft LWCs tend to be similar to the median SCM values but are larger than the CRM median values. However, the aircraft sampled the cloud only over open ocean while the models treated the surface as land; thus, it is not surprising that the modeled clouds contain less water. In contrast, the modeled values of liquid water path (LWP) are smaller than the ground-based retrievals as described below.

Because the observations (both from the aircraft and radar retrievals) do not distinguish between cloud and precipitation ice, the models must include both cloud and precipitation ice (snow and graupel) for a consistent comparison (note that in many models precipitation ice is a significant fraction of the total ice). In models with bulk microphysics, the partitioning between cloud and precipitation ice is rather arbitrary, despite the fact that this issue is important since models typically only include radiative effects of the cloud ice. In some of the SCM simulations, precipitation ice contents were not reported (ECHAM, GISS, MCRAS, MCRASI, NCEP, SCRIPPS). These models are therefore not included in the comparison with the observed IWC.

There is little difference in the median values of IWC for the SCMs and CRMs, although there is a large spread among the individual models (Figure 7a). The model median IWC profile is similar to the aircraft observations and radar retrievals in terms of its distribution with height (i.e., the decrease of IWC with greater height), although the model values are consistently smaller by a factor of 2-3 (Figure 7b). The radar-derived and aircraft profiles of IWC are generally similar, although there is considerable temporal variability associated with both values. However, the variability of IWC between aircraft

flights is less than it is for the LWC. Some of the differences between the aircraft and retrieved IWC may result from sampling by aircraft over ocean versus ground-based retrievals over land.

d) *Hydrometeor number concentrations and effective radii*

The aircraft observed droplet concentrations are generally between 10 and 40 cm^{-3}, and do not exhibit any clear trend with height (see Fig. 11 in Luo et al. 2008b). The average droplet effective radius is between 8 and 13 μm. The aircraft observed crystal concentrations (for particles larger than 53 μm) have significant variability over time and height, with average concentrations for each flight generally less than 10 L^{-1}, although on Oct. 8 the mean concentration in the lower part of the cloud exceeded 80 L^{-1} (see Fig. 13 in Luo et al. 2008b). The average ice effective radius is between 23 and 26 μm and is fairly constant with height. There are substantial intermodel differences in the particle number concentrations and effective radii. However, much of this variability is the result of models coupling with different aerosol characteristics. For models that did couple with M-PACE aerosol (ARCSCM, UCLA-LARC, ECHAM), the droplet number concentrations and effective radii are similar to observations, generally ranging between 10 to 50 cm^{-3} and 8 to 15 μm, respectively. However, there is no evidence that coupling with M-PACE aerosol produces better overall simulation in terms of liquid and ice water paths, cloud fraction, cloud radiative forcing, etc. A similar conclusion was reached for the single-layer case in Part I. For ice, the number concentration (cloud ice plus snow) and effective radius vary widely even among the simulations that were coupled with the observed ice nucleus concentrations.

e) *Liquid and ice water paths*

The retrieved domain-average liquid and ice water paths, averaged from 000 UTC Oct. 6 to 1400 UTC Oct. 8, are shown in Table 2. The modeled values are shown in Table 3. The retrieved and modeled time-average values of LWP as a function of the IWP are shown in Figure 8. Uncertainty in the retrieved LWP is illustrated by the range of values using different retrieval method and measurement locations (see Table 2). Nonetheless, intermodel differences far exceed the retrieval uncertainty; there is approximately a factor of 10 spread in average LWP among the models. Ten of the seventeen models produce a time-average LWP larger than the mean retrieved value, with the median model value somewhat larger than retrieved.

The median LWP for models with two-moment microphysics is somewhat smaller than the median for models with one-moment microphysics (both single-moment with T-dependent partitioning and with independent liquid and ice). Thus, models with two-moment microphysics tend to produce a mean LWP that is slightly closer to the retrieved values (although there is considerable scatter). This point is reinforced by the simulations which use different microphysics schemes in otherwise the same model; there is a reduced LWP produced by the two-moment schemes of SCAM3-LIU and SCAM3-MG relative to SCAM3 which employs a one-moment scheme (155 and 136 versus 298 g m^{-2}), and MCRASI relative to MCRAS (44 versus 83 g m^{-2}). There is little difference in median LWP between the SCMs and CRMs. However, the UCLA-LARC CRM has a smaller LWP compared to the ARCSCM SCM (82 versus 199 g m^{-2}), even though both models use the same two-moment microphysics scheme.

In contrast to the LWP, the models tend to strongly underpredict IWP relative to the radar retrievals (even considering only those models that include both cloud and precipitation ice). On the face of it, this suggests too little conversion of liquid to cloud and/or precipitating ice. Models with two-moment microphysics schemes tend to produce smaller IWP than those with one-moment schemes, resulting in an even more substantial undeprediction of IWP relative to the retrieved value. It should be kept in mind that there is considerable uncertainty in the retrieved IWP; the model median IWP (considering only models that include cloud and precipitation ice) is at the limit of the factor of two estimate of uncertainty in the retrieved value. There is considerable spread of IWP among the models, although much of this difference is due to the exclusion of precipitation ice in some of the models. For models that include both cloud and precipitation ice, there is still a factor of 5 spread in the IWP, but this is less than the spread of LWP among the same models. In these models, the cloud ice water path is less than 20% of the total IWP (i.e., including cloud ice, snow, and graupel), with a few exceptions (ARCSCM, CCCMA, SAM, UCLA-LARC). Similar to Part I, nearly all of the precipitating ice mass is represented by snow rather than graupel in the models that include both species.

Timeseries of the modeled median and retrieved LWP and total IWP are shown in Figure 9. For median IWP, only the models that reported both cloud and precipitation ice are included. The overprediction of LWP and underprediction of IWP seen in the time-averages occurs primarily on Oct. 6 and the first half of Oct. 7, when deeper clouds extending to mid-levels predominated in the real atmosphere (see Fig. 2). During the brief period at the end of Oct. 7 and first few hours on Oct. 8, when a single-layer, low-level cloud was observed, the models underestimate LWP and overestimate IWP,

consistent with results for the single-layer case in Part I. In the observations, the transition from a deep, multi-layer cloud to low-level single-layer cloud at the end of Oct. 7 was marked by sharply increasing LWP and decreasing IWP to values similar to the low-level cloud in Part I, suggesting that seeding of the lower-level cloud from above may have reduced its LWP earlier in the period.

There is little correlation between the number of mixed-phase layers in the vertical, and the mean LWP or IWP produced by the models. Thus, capturing the detailed multi-layered structure appears to have limited impact on vertically-integrated amounts of cloud water and ice.

f) *Surface precipitation*

Ice fell to the surface intermittently during the period in the form of light snow. Unfortunately, quantitative estimates of the surface snow rate are highly uncertain due to factors such as blowing snow and because of the small precipitation amounts. The National Weather Service station in Barrow recorded an average precipitation rate of 0.7 mm/day; however, the ARM precipitation rate measured at Barrow was a factor of 7 larger. The total precipitation rate in the simulations, averaged from 000 UTC Oct. 6 to 1400 UTC Oct. 8, varies widely with the largest value of 1.62 mm/day in ECHAM and the smallest value of 0.34 mm/day in CCCMA. Most of the models produced primarily frozen precipitation (snow), but in several simulations the majority of the surface precipitation was liquid (ECHAM, SCAM3, SCAM3-LIU, MCRAS, MCRASI, RAMS-CSU, NCEP).

g) *Thermodynamic profiles*

Intermodel differences in the temperature, averaged between 000 UTC Oct. 6 and 1400 UTC Oct. 14, are rather small (maximum of ~ 5 K over the depth of the profile) (Figure 10). The median values for the different model ensembles are close to observations (within 2 K), with the CRM median slightly colder than the SCM median. Intermodel differences in the time-average water vapor mixing ratio profiles are also small (maximum of ~ 0.6 g/kg over the depth of the profile) (Figure 11). The median values for different model ensembles are close to observations (within 0.3 g/kg), with the CRM median value slightly drier between 600 and 900 mb compared to the SCM median, consistent with the slightly colder median temperature. The spread among models and error relative to observations for the temperature and water vapor profiles are considerably less than previous model intercomparisons of deep and shallow midlatitude frontal clouds (see Fig. 14 in Xie et al. 2005; Fig. 10 in Xu et al. 2005). These results also indicate that the substantial intermodel differences in cloud fraction and condensate amount are not associated with large differences in the thermodynamic profiles.

h) *Radiative fluxes*

In the Arctic, the downward component of the surface radiation is strongly affected by clouds and is an important quantity that affects the surface temperature of land and sea ice. Although this effect is disabled in the model simulations here, it is important to assess whether the modeled clouds have the correct radiative impacts.

Despite the general overprediction of LWP, several models produce a time-average surface downwelling longwave (LW) flux that is reasonably close to

observations (Figure 12). This occurs because the LW flux saturates at a mean LWP greater than about 50 – 75 g m^{-2}, so that the clouds tend to emit as blackbodies and further increase in condensate amount has little impact (Stephens 1978). Conversely, models that produce a mean LWP less than 50 – 75 g m^{-2} underpredict the LW flux. Ice has less impact on downwelling radiative fluxes because of the dominance of cloud water mass relative to cloud ice in nearly all of the models.

The relationship between surface downwelling LW and column cloud fraction is shown in Fig. 12b. Here, column cloud fraction is calculated by assuming maximum overlap in the vertical (note that this overlap assumption is not necessarily employed for radiative calculations in all of the models but is used here for simplicity to illustrate the key points). Not surprisingly, downwelling LW flux increases steadily with greater column cloud fraction. All of the CRMs produce a mean column cloud fraction close to 100%, while the SCMs produce values ranging from 62 – 100%. Several of the SCMs produce a small column cloud fraction (< 90%), consistent with the smaller median SCM cloud fraction compared with the median CRM value described previously. These differences in cloud fraction explain much of the intermodel difference in downwelling LW, especially for models that produce a mean LWP exceeding 50 – 75 g m^{-2}. For example, SCAM3, which has the largest mean LWP of all models, produces one of the smallest mean downwelling LW fluxes because of the relatively low mean column cloud fraction (73%). On the other hand, METO has a column cloud fraction of nearly 100%, but has the second lowest mean downwelling LW flux among all models because of the small mean LWP (26 g m^{-2}). These results highlight the importance of both cloud fraction and condensate amount in determining the LW fluxes. Because all of the models produce

clouds at low levels and the temperature profiles among the simulations are similar, differences in cloud emission temperature appear to not be as significant in explaining differences in surface LW flux.

The time-averaged downwelling solar (SW) flux at the surface decreases with increasing LWP and column cloud fraction as expected, although there is considerable scatter (Fig. 13). The observed SW flux is in the middle range of the model values. Note that for this case the time-average downwelling SW flux is about an order of magnitude smaller than the LW flux due to the high zenith angle and extended periods of darkness. The modeled upwelling top-of-atmosphere (TOA) radiative fluxes also exhibit differences consistent with the column cloud fraction (and less so with the mean LWP), although the spread among models is less for the TOA LW flux than the downwelling surface LW flux (not shown). Nearly all of the models underestimate the LW TOA flux due to the unrealistic presence of upper-level ice clouds on Oct. 7 and 8.

7. Sensitivity tests

a) *No ice microphysics*

Prior modeling studies have suggested the sensitivity of mixed-phase clouds to representation of ice microphysics (e.g., Pinto 1998; Morrison and Pinto 2006; Prenni et al. 2007). This sensitivity is examined here with additional simulations in which all ice processes were turned off. All of the models except GISS, SCAM3, SCAM3-LIU, and SCAM3-MG ran this test, which allows us to examine the role of ice in depleting liquid water in the simulations.

The average LWP for each model over the period 000 UTC Oct. 6 to 1400 UTC Oct. 8 for the sensitivity test without ice as a function of the baseline LWP is shown in Figure 14. As expected, LWP increases in the simulations without ice, although this increase is quite small for some models (especially ECHAM). Other models show a substantial increase in LWP without ice microphysics (GISS, METO, MCRASI, UWM). This suggests that the relatively small mean baseline LWP produced by three of these four models (METO, GFDL, MCRASI) is mostly due to their greater depletion of liquid water by ice relative to the other models. The three CRMs with 2-moment microphysics (RAMS-CSU, UCLA-LARC, METO) all produce similar LWP without ice microphysics (ranging from 180 to 245 g m^{-2}), even though they differ greatly for the baseline simulations with ice (ranging from 26 to 170 g m^{-2}). Some of the differences in the amount of liquid depleted by ice are directly attributable to differences in the temperature based partitioning between liquid and ice in the models with the most simplified treatment of the microphysics (NCEP, SAM, SCAM3).

Time-averaged median values of LWP for the ice-free simulations are shown in Table 3. In contrast to the baseline results, the CRM median LWP is smaller than the SCM median value in the runs without ice. The median value of the models with 2-moment microphysics is less than the value of the models with 1-moment microphysics, similar to the baseline simulations.

b) *Increased vertical resolution*

As described in Part I, low vertical resolution in models may lead to non-convergence of simulated cloud properties, especially for the fairly thin mixed-phase

layers for this case. To explore this issue, all of the models except for SCAM3-MG and GISS ran sensitivity tests with increased vertical resolution. The participants chose how much to increase the vertical resolution (see Table 1).

Figure 15 shows the LWP from the high resolution run, averaged over the period 000 UTC Oct. 6 to 1400 UTC Oct. 8, as a function of the average baseline LWP for each model. Values for each model are also shown in Table 3. The mean high-resolution LWP is within a factor of 2 or less of the baseline LWP for all of the models. Interestingly, increasing the resolution leads to an increase in LWP for many of the models that produce smaller LWP for the baseline run; conversely, it leads to a decrease in LWP for many of the models that produce larger baseline LWP. Excluding the models with the simplest treatment of microphysics (single-moment with T-based partitioning of liquid and ice in NCEP, SAM, SCAM3) and the METO outlier, the spread among the models for the high resolution runs is 82 g m^{-2} in MCRASI to 198 g m^{-2} in CCCMA. The same models produce a much larger spread in baseline LWP, ranging from 49 g m^{-2} in MCRASI to 278 g m^{-2} in SCRIPPS. Thus, there is evidence suggesting that increasing the vertical resolution improves the convergence of LWP among models, as long as they have a reasonably sophisticated treatment of the microphysics (at least one-moment with separate treatment of liquid and ice), with the exception of the METO model. In contrast, there were no consistent trends in the high resolution simulations noted for the single layer case in Part I. In general, the IWP exhibits limited sensitivity to the vertical resolution (with the exception of MCRASI) (see Table 3).

Interestingly, the increase in vertical resolution has a limited impact on the macrophysical structure and multi-layering of mixed-phase regions (not shown). This

finding is consistent with the baseline results that show no consistent trend in terms of multi-layering between models with lower and higher vertical resolution.

8. Discussion and conclusions

This modeling study extensively compared simulations from 13 SCMs and 4 CRMs of a case study of a deep, multi-layered, mixed-phase stratiform cloud system observed during M-PACE on Oct. 5-8. This cloud formed by surface forcing via large turbulent heat and moisture fluxes over the open ocean combined with a weak, mid-level low pressure system. A unique feature of this case is the presence of multiple liquid layers in the vertical, with ice precipitation falling between the layers and intermittently reaching the surface as light snow.

The models were able to reasonably reproduce the cloud macrophysical structure, consisting of a persistent boundary layer cloud and intermittent mid-level cloudiness, although there were significant intermodel differences in cloud fraction. Nearly all of the models produced unrealistic upper-level ice clouds on Oct. 7 and 8, which may have resulted from biases in the large-scale forcing. In general, the SCMs produced smaller cloud fraction than the CRMs, in contrast to model results from more strongly-forced cases of shallow and deep midlatitude frontal systems that showed no consistent differences between SCM and CRM cloud fraction (Xie et al. 2005; Xu et al. 2005). However, we also note that these previous studies used larger condensate thresholds to define cloud fraction in the CRMs, which could account for some of the difference. Large intermodel differences in cloud fraction as well as condensate amount were not associated with significant differences in the temperature or water vapor profiles.

All of the models except one were able to produce multiple layers of liquid in the mixed-phase clouds as were observed, suggesting that the occurrence of multi-layering was more a result of the large-scale atmospheric and surface forcing than details of the model physics. Although nearly all of the models produced some multi-layering, the actual number of layers varied widely among the models and, surprisingly, was not correlated with the vertical resolution. The number of layers was also poorly correlated with other key cloud quantities such as LWP and IWP.

In the Arctic, the downward component of the surface radiation is a critical quantity that affects the surface temperature of land and sea ice (although this effect was not included here). Differences in the cloud fraction were key in producing intermodel variability in the downwelling surface LW fluxes (as well as the SW fluxes, although they were considerably smaller on average than the LW fluxes). Several of the SCMs produced a small column cloud fraction (< 90%) and thus small downward LW flux. These results highlight the need for a realistic simulation of cloud fraction in order to produce the correct cloud forcing at the surface in the Arctic. Differences in LWP were comparatively less important for the downwelling LW flux because several of the models produced a mean LWP greater than 50 – 75 g m^{-2}, meaning that the clouds tended to emit as near-blackbodies. However, LWP had a large impact on the downwelling surface LW fluxes in models with a mean LWP less than 50 – 75 g m^{-2}. The impact of the cloud ice water path on the radiative fluxes was secondary, since cloud liquid was dominant in nearly all of the models.

The majority of models overpredicted the mean observed LWP, especially relative to the TURNER retrievals, and underpredicted the mean IWP. This finding is in

sharp contrast to results from the low-level single-layer case in Part I, as well as previous modeling studies of Arctic mixed-phase stratus that have reported a substantial *under-prediction* of LWP by models (Curry et al. 2000; Girard and Curry 2001; Morrison et al. 2003; Morrison and Pinto 2006; Inuoue et al. 2006; Prenni et al. 2007). Underprediction of LWP was also noted by Xie et al. (2005) and Xu et al. (2005) in simulations of mid-latitude frontal clouds. We note that there is an inconsistency in the lower boundary between Part I (surface treated as ocean) and here (surface treated as mostly land). However, assuming an open ocean surface with larger turbulent heat fluxes here would likely exaggerate the overprediction of LWP. Conversely, assuming a land surface with smaller fluxes in Part I would likely exaggerate the underprediction of LWP found in that study. Thus, our conclusion that the models tend to overpredict LWP here and underpredict it for the single-layer case in Part I is likely not due to the difference in surface conditions.

An analysis of the LWP timeseries suggested that most of the overprediction of LWP occurred during episodes of deeper cloud that extended into the mid-troposphere. At the end of Oct.7 and first few hours of Oct. 8, when only a low-level, shallow cloud was present, the models tended to underpredict LWP and overpredict IWP consistent with results from Part I. The observed LWP (IWP) associated with this low-level, single-layer cloud on Oct. 7 and 8 was much higher (lower) than earlier in the period when deeper clouds predominated. This suggests the impact of seeding of ice from above in reducing LWP in the deeper clouds.

These results suggest that the models behave quite differently for deeper mixed-phase clouds compared to low-level, shallow mixed-phase clouds. In Part I, results

suggested that the conversion from liquid to ice was too rapid. The results here seem to suggest the opposite; that is, in general the models were unable to convert enough liquid to ice. This key difference between the results here and in Part I is potentially explained by the different ice formation mechanisms occurring in shallow, single-layer clouds compared with deeper mixed-phase clouds. In deeper clouds, ice growth via riming and depositional growth may deplete liquid water as crystals fall into the layer ("seeder-feeder" process), while in shallow clouds this process is likely to be much less effective. This was evident from the observations, as the LWP increased sharply (and IWP decreased sharply) during the transition from deep, multi-layered cloud to shallow cloud on Oct. 7. Thus, models that are able to realistically capture ice formation in one regime may fail in the other. This may be especially true of models with a simple treatment of the microphysics, such as single-moment schemes with temperature-dependent partitioning, since they cannot capture different physical processes that occur at similar temperatures.

Although the models tended to overestimate LWP and underestimate IWP, there were large intermodel differences in both quantities. This variability may have had several major causes. First, there was a large spread among the models in terms of how much cloud liquid water was depleted by the ice. Some of this spread was directly attributable to differences in the temperature-based partitioning between liquid and ice in the models with the most simplified treatment of the microphysics (NCEP, SAM, SCAM3). Differences in the boundary layer parameterizations may have also had a large impact on the lower-level cloud layers. The order of magnitude spread in LWP among models here was roughly similar to the spread of LWP found in LES and SCM model

intercomparisons of warm marine stratocumulus (Stevens et al. 2005; Zhu et al. 2005), as well as the single-layer mixed-phase case in Part I. Large intermodel differences in the amount of cloud liquid and ice condensate were also noted in simulations of mid-latitude frontal clouds (Xie et al. 2005; Xu et al. 2005). Here, increasing the vertical resolution significantly decreased the spread of LWP among those models with a more sophisticated treatment of the microphysics (1-moment with separate treatment of liquid and ice, or 2-moment).

Overall, models using 2-moment instead of 1-moment microphysics schemes produced a somewhat lower LWP that was closer to observations. This difference was even more evident in the simulations without ice, and therefore was not a direct result of differences in the microphysical conversion of liquid to ice. For the low-level single-layer case in Part I, it was found that models with two-moment microphysics schemes tended to produce *greater* amounts of liquid water that were closer to observations than models with one-moment microphysics. Thus, models with two-moment schemes produced results closer to observations in terms of LWP both here and in Part I, even though here they produced less liquid water than models with one-moment schemes, and in Part I they produced more liquid water. However, we emphasize that there is considerable scatter among the simulations; thus, caution is needed when interpreting these results. We also note that here models with one-moment schemes tended to produce larger IWP that was closer to the retrieved value, although the retrieved IWP has considerable uncertainty and the IWP has less impact on the cloud forcing at the surface compared to the LWP. It is possible that some of these differences using one- or two-moment microphysics schemes may be more related to the details of the schemes, rather than more broadly the number

of moments predicted. Further explanation for these differences will require additional study at the process level.

We emphasize that the generalization of these results to other cases is uncertain. Nevertheless, the availability of this observationally well-constrained case study, along with that from Part I, adds to the growing number of such datasets and should be valuable for individual modelers to further improve their cloud and cloud microphysics parameterizations.

Acknowledgments. This work is supported by the Office of Science of the United States Department of Energy under grants DE-FG02-02ER63337 (McFarquhar), DE-FG02-03ER63539 (Morrison), DE-FG02-05ER64058 (Harrington), DE-FG02-05ER64069 (Wang), DE-FG02-06ER64167 (Turner), and DE-FG02-07ER64378 (McFarquhar). J. Cole is supported by the Canadian Foundation for Climate and Atmospheric Sciences. M. Falk and V. Larson are supported by National Science Foundation grant ATM-0442605 and subaward G-7424-1 from the Department of Defense Center for Geosciences/Atmospheric Research at Colorado State University via Cooperative Agreement DAAD19-02-2-0005 with the Army Research Laboratory. C. Hoose is supported by the climate program of the Swiss National Centre of Competence in Research. Y. Luo is supported by the Chinese Academy of Meteorological Sciences and the United States National Aeronautics and Space Administration's Cloud Modeling and Analysis Initiative. H. Morrison is supported by NASA grant NNG06GBB1G and by the NSF Science and Technology Center for Multi-Scale Modeling of Atmospheric Processes, managed by Colorado State University under cooperative agreement ATM-

0425247. The contribution of S. Klein, R. McCoy, and S. Xie to this work is performed under the auspices of the U. S. Department of Energy by Lawrence Livermore National Laboratory under contract DE-AC52-07NA27344. X. Liu acknowledges that the Pacific Northwest National Laboratory is operated for the Department of Energy by Battelle Memorial Institute under contract DE-AC06-76RLO-1830. National Center for Atmospheric Research is sponsored by the National Science Foundation..

References.

Clothiaux, E. E., T. P. Ackerman, G. G. Mace, K. P. Moran, R. T. Marchand, M. Miller, and B. E. Martner, 2000: Objective determination of clouds heights and radar reflectivities using a combination of active remote sensors at the ARM CART sites. *J. Appl. Meteor.*, **39**, 645-665.

Curry, J. A., 1986: Interactions among turbulence, radiation, and microphysics in Arctic stratus clouds. *J. Atmos. Sci.*, **43**, 90-106.

Curry, J. A., E. E. Ebert, and G. F. Herman, 1988: Mean and Turbulent structure of the summertime Arctic cloudy boundary layer. *Quart. J. Roy. Meteor. Soc.*, **114**, 715-746.

Curry, J. A., W. B. Rossow, and J. L. Schramm, 1996: Overview of arctic cloud and radiation properties, *J. Climate*, *9*, 1731-1764.

Curry, J. A., and Coauthors, 2000: FIRE Arctic Clouds Experiment, *Bull. Amer. Meteor. Soc.*, **81**, 5-29.

Eloranta, E. W., 2005: High Spectral Resolution Lidar, in *Lidar: Range-Resolved Optical Remote Sensing of the Atmosphere*, K. Weitkamp, Ed., Springer-Verlag, 143-163.

Fleishauer, R. P., V. E. Larson, and T. H. Vonder Haar, 2002: Observed microphysical structure of mid-level, mid-latitude clouds. *J. Atmos. Sci.*, **59**, 1779-1804.

Fridlind, A. M., A. S. Ackerman, G. McFarquhar, and G. Zhang, M. R. Poellot, P. J. DeMott, A. J. Prenni, and A. J. Heymsfield, 2007: Ice properties of single-layer stratocumulus during the Mixed-Phase Arctic Cloud Experiment (M-PACE): Part II: Model results. *J. Geophys. Res.*, **112**, D24202, doi:10.1029/2007JD008646.

Fu, Q., 1996: An accurate parameterization of the solar radiative properties of cirrus clouds, *J. Climate*, **9**, 2058-2082.

Girard, E., and J. A. Curry, 2001: Simulation of Arctic low-level clouds observed during the FIRE Arctic Clouds Experiment using a new bulk microphysics scheme. *J. Geophys. Res.*, **106**, 15139-15154.

Harrington, J. Y., T. Reisin, W. R. Cotton, and S. M. Kreidenweis, 1999: Cloud resolving simulations of Arctic stratus. Part II: Transition-season clouds. *Atmos. Res.*, **55**, 45-75.

Herman, G. F., and R. Goody, 1976: Formation and persistence of summertime Arctic stratus clouds. *J. Atmos. Sci.*, **33**, 1537-1553.

Inoue, J., J. Liu, J. O. Pinto, and J. A. Curry, 2006: Intercomparison of Arctic regional climate models: Modeling clouds and radiation for SHEBA in May 1998. *J. Clim.*, **19**, 4167-4178.

Intrieri, J. M., M. D. Shupe, T. Uttal, and B. J. McCarty (2002), An annual cycle of Arctic cloud characteristics observed by radar and lidar at SHEBA, *J. Geophys. Res.*, **107**, 8030, doi:10.1029/2000JC000423.

Jayaweera, K. O. L. F., and T. Ohtake, 1973: Concentration of ice crystals in Arctic stratus clouds. *J. Rech. Atmos.*, **7**, 199-207.

Klein, S., and Coauthors, 2008: Intercomparison of model simulations of mixed-phase clouds observed during the ARM Mixed-Phase Arctic Cloud Experiment. Part I: Single layer cloud. *Quart. J. Roy. Meteor. Soc.* (submitted)

Liu, X., S. Xie, and S. J. Ghan, 2007: Evaluation of a new mixed-phase cloud microphysics parameterization with CAM3 single-column model and M-PACE observations. *Geophys. Res. Lett.*, **34**, L23712, doi:10.1029/2007GL031446.

Luo, Y., K.-M. Xu, H. Morrison, and G. McFarquhar, 2008a: Arctic mixed-phase clouds simulated by a cloud-resolving model: Comparison with ARM observations and sensitivity to microphysics parameterization. *J. Atmos. Sci.* (in press)

Luo, Y., K.-M. Xu, H. Morrison, G. McFarquhar, Z. Wang, and G. Zhang, 2008b: Multi-layer Arctic mixed-phase clouds simulated by a cloud-resolving model: Comparison with ARM observations and sensitivity experiments. *J. Geophys. Res.* (accepted)

McFarquhar, G. M., G. Zhang, M. Poellot, J. Verlinde, G. Kok, R. McCoy, T. Tooman, A. Fridlind and A. J. Heymsfield, 2007a: Ice properties of single layer boundary clouds during the Mixed-Phase Arctic Cloud Experiment (MPACE): Part I Observations. *J. Geophys. Res*., **112**, D24201, doi:10.1029/2007JD008633.

McFarquhar, G. M., J. Um, M. Freer, D. Baumgardner, G. L. Kok, and G. Mace, 2007b: The importance of small crystals to cirrus properties: Observations from the Tropical Western Pacific International Cloud Experiment (TWP-ICE). *Geophys. Res. Lett.*, **34**, L13803, doi:10.1029/2007GL029865.

Morrison, H., M. D. Shupe, and J. A. Curry, 2003: Modeling clouds observed at SHEBA using a bulk parameterization implemented into a single-column model. J. *Geophys. Res.*, **108**, doi:10.1029/2002JD002229.

Morrison, H., and J. O. Pinto, 2006: Intercomparison of bulk cloud microphysics schemes in mesoscale simulations of springtime arctic mixed-phase stratiform clouds, *Mon. Wea. Rev.*, **134**, 1880-1900.

Morrison, H., J. O. Pinto, J. A. Curry, and G. McFarquhar, 2008: Sensitivity of modeled Arctic mixed-phase stratocumulus to cloud condensation and ice nuclei over regionally-varying surface conditions. *J. Geophys. Res.* (in press)

Pinto, J. O., 1998: Autumnal mixed-phase cloudy boundary layers in the Arctic, *J. Atmos. Sci.*, **55**, 2016-2038.

Prenni, A. J., J. Y. Harrington, M. Tjernstrom, P. J. DeMott, A. Avramov, C. N. Long, S. M. Kreidenweis, P. Q. Olsson, and J. Verlinde, 2007: Can ice-nucleating aerosols affect Arctic seasonal climate?, *Bull. Amer. Met. Soc.*, **88**, 541-550.

Randall, D. A. and Coauthors, 2003: Confronting models with data: The GEWEX Cloud Systems Study. *Bull. Amer. Met. Soc.*, **84**, 455–469.

Shupe, M. D., and J. M. Intrieri, 2004: Cloud radiative forcing of the Arctic surface: The influence of cloud properties, surface albedo, and solar zenith angle, *J. Climate*, **17**, 616-628.

Shupe, M. D., S. Y. Matrosov, and T. Uttal, 2006: Arctic mixed-phase cloud properties derived from surface-based sensors at SHEBA. *J. Atmos. Sci.*, **63**, 697–711.

Shupe, M. D., 2007: A ground-based multiple remote-sensor cloud phase classifier. *Geophys. Res. Lett.*, **34**, L22809, doi:10.1029/2007GL031008.

Stephens, G. L., 1978: Radiation profiles in extended water clouds, II: Parameterization schemes. *J. Atmos. Sci.*, **35**, 2123-2132.

Stevens, B. and Coauthors, 2005: Evaluation of large-eddy simulations via observations of nocturnal marine stratocumulus. *Mon. Wea. Rev.*, **133**, 1443–1462.

Sun, Z., and K. Shine, 1994: Studies of the radiative properties of ice and mixed-phase clouds. *Quart. J. Roy. Meteor. Soc.*, **120**, 111-137.

Tsay, S.-C., and K. Jayaweera, 1984: Physical characteristics of Arctic stratus clouds. *J. Climate Appl. Meteor.*, **23**, 584-596.

Turner, D. D., 2005: Arctic mixed-phase cloud properties from AERI-lidar observations: Algorithms and results from SHEBA. *J. Appl. Meteor.*, **44**, 427-444.

Turner, D. D., S. A. Clough, J. C. Liljegren, E. E. Clothiax, K. Cady-Pereira, and K. L. Gaustad, 2007: Retrieving liquid water path and precipitable water vapor from the Atmospheric Radiation Measurement (ARM) microwave radiometers, *IEEE Trans. Geosci. Remote Sens.*, **45**, 3680-3690.

Verlinde, H., and Coauthors, 2007: The Mixed-Phase Arctic Cloud Experiment (M-PACE). *Bull. Amer. Meteor. Soc.*, **88**, 205-221.

Wang, Z., and K. Sassen, 2001: Cloud type and macrophysical property retrieval using multiple remote. *J. Appl. Meteor.*, **40**, 1665-1682.

Wang, Z., 2007: A refined two-channel microwave radiometer liquid water path retrieval for cold regions by using multiple-sensor measurements, *IEEE Geo. Rem. Sens. Lett.*, **4**, 591-595.

Xie, S., and Coauthors, 2005: Simulations of midlatitude frontal clouds by single-column and cloud-resolving models during the Atmospheric Radiationo Measurement March 2000 cloud intensive operation period. *J. Geophys. Res.*, **110**, doi:10.1029/2004JD005119.

Xie, S., S. A. Klein, M. Zhang, J. J. Yio, R. T. Cederwall, and R. McCoy, 2006: Developing large-scale forcing data for single-column and cloud-resolving models from the Mixed-Phase Arctic Cloud Experiment. *J. Geophys. Res.*, **111**, doi:10.1029/2005JD006950.

Xie, S., J. Boyle, S. A. Klein, X. Liu, and S. J. Ghan, 2008: Simulations of Arctic mixed-phase clouds in forecasts with CAM3 and AM2 for M-PACE. *J. Geophys. Res.* (in press).

Xu, K.-M., and Coauthors, 2005: Modeling springtime shallow frontal clouds with cloud-resolving and single-column models. *J. Geophys. Res.*, **110**, doi:10.1029/2004JD005153.

Zhu P. and Coauthors, 2005: Intercomparison and interpretation of single-column model simulations of a nocturnal stratocumulus-topped marine boundary layer. *Mon. Wea. Rev.*, **133**, 2741-2758.

Zuidema, P., and Coauthors, 2005: An Arctic springtime mixed-phase cloudy boundary layer observed during SHEBA. *J. Atmos. Sci.*, **62**, 160-176.

Table 1. Number of vertical levels in the participating models for both the baseline and sensitivity simulation with increased vertical resolution.

Model Name	*Model Type*	*Number of levels – Baseline*	*Number of level – Sensitivity*
ARCSCM	SCM	30	59
CCCMA	SCM	35	50
ECHAM	SCM	31	98
GFDL	SCM	24	96
GISS	SCM	35	-
McRAS	SCM	17	137
McRASI	SCM	17	137
NCEP	SCM	64	640
SCAM3	SCM	26	60
SCAM3-MG	SCM	26	-
SCAM3-LIU	SCM	26	60
SCRIPPS	SCM	20	53
UWM	SCM	100	500
RAMS-CSU	CRM	52	71
SAM	CRM	45	69
UCLA-LARC	CRM	45	99
METO	CRM	45	81

Table 2. Retrieved liquid water path (LWP) and ice water path (IWP) from ground-based remote sensing, averaged during the period 000 UTC Oct. 6 to 1400 UTC Oct. 8.

Retrieval Method	Location	LWP (g m-2)	IWP (g m-2)
WANG	Barrow	121	-
WANG	Oliktok Point	119	-
TURNER/ TURNER-SHUPE	Barrow	116	81
TURNER	Oliktok Point	58	-
TURNER	Atqasuk	55	-

Table 3. Modeled liquid water path (LWP) and ice water path (IWP) for the baseline and sensitivity tests with no ice microphysics and increased vertical resolution. '1-M T-dep', '1-M Ind', and '2-M' refer to the models using one-moment microphysics schemes with T-dependent partitioning, one-moment schemes with independent liquid and ice, and two-moment schemes, respectively. Asterisk (*) indicates models that did not include precipitation ice. Median IWP values are derived only from models that include both cloud and precipitation ice.

Model/Ensemble	LWP (g m^{-2})			IWP (g m^{-2})	
	Baseline	High Vert. Resolution	No Ice	Baseline	High Vert. Resolution
Median model	123	125	332	42	43
Median SCM	123	121	452	42	48
Median CRM	126	128	230	38	34
Median 1-M T-dep	147	127	332	48	49
Median 1-M Ind	123	172	693	42	63
Median 2-M	115	117	230	27	26
ARCSCM	199	197	452	28	26
CCCMA	182	220	216	62	83
ECHAM	93	166	97	1.9*	1.7*
GFDL	65	102	717	42	42
GISS	109	-	-	37*	-
McRAS	83	128	332	3.5*	4.5*
McRASI	44	81	504	5.8*	18*
NCEP	30	27	87	36*	34*

Model/Ensemble	LWP (g m^{-2})			IWP (g m^{-2})	
	Baseline	High Vert. Resolution	No Ice	Baseline	High Vert. Resolution
SCAM3	298	334	-	42	55
SCAM3-MG	136	-	-	21	-
SCAM3-LIU	155	105	-	87	121
SCRIPPS	245	162	668	20*	22*
UWM	123	103	1448	36	31
RAMS-CSU	170	184	215	13	20
SAM	211	125	793	54	43
UCLA-LARC	82	117	245	49	51
METO	26	20	180	26	25

List of figure captions.

Figure 1. Map of the M-PACE analysis domain (region bounded by A1-A6) and location of the surface observing sites.

Figure 2. Time-height plot of the ARSCL-derived cloud fraction (%).

Figure 3. Example of an aircraft profile of liquid water potential temperature, θ_l (solid), liquid water content (dotted), ice water content (dash), observed during an ascent spiral at about 1917 UTC on Oct. 6.

Figure 4. Time-height plot of the large-scale total advective tendencies of temperature and water vapor mixing ratio.

Figure 5. a) Time-averaged cloud fraction from observations and models as a function of height. The properties depicted are a) the median of the models (solid line), the inner 50% (dotted line), and the min/max (dashed line); b) the ARSCL observations (thick solid line with thin solid line indicated +/-1 st. dev.) and median of the SCMs and CRMs. The averaging period is from 000 UTC Oct. 6 to 1400 UTC Oct. 8.

Figure 6. a) Time-averaged liquid water content from observations and models as a function of height. The properties depicted are a) the median of the models (solid line), the inner 50% (dotted line), and the min/max (dashed line); b) the aircraft observations (thick solid line with thin solid line indicating +/-1 st. dev.) and median of the SCMs and CRMs. The averaging period is from 000 UTC Oct. 6 to 1400 UTC Oct. 8 for the simulations. The aircraft value is the average of three flights that occurred on Oct. 5, 6, and 8.

Figure 7. a) Time-averaged ice water content from observations and models as a function of height. The properties depicted are a) median of the models (solid line), the inner 50% (dotted line), and the min/max (dashed line); b) the aircraft observations 'AIR' (thick solid line with thin solid line indicating +/-1 st. dev.), SHUPE-TURNER radar retrievals 'RET' (thick dot-dash line with thin dot-dash line indicating +/-1 st. dev.), and median of the SCMs and CRMs. The averaging period is from 000 UTC Oct. 6 to 1400 UTC Oct. 8 for the simulations and radar retrievals. The aircraft value is the average of three flights that occurred on Oct. 5, 6, and 8.

Figure 8. Time-averaged ice water path (IWP) as a function of liquid water path (LWP) for the models and ground-based retrievals. Symbols plotted for each model indicate type (SCM versus CRM) and cloud microphysics scheme (one-moment with T-dependent partitioning "1-M, T-dep", one-moment with independent liquid and ice "1-M, Ind", and two-moment "2-M"). "Cloud ice only" indicates the models that did not report precipitation ice. "T" and "W" indicate LWP retrievals using the TURNER method averaged between Barrow, Oliktok, and Atqasuk, and WANG method averaged between Barrow and Oliktok, respectively, and retrieved IWP using the SHUPE-TURNER method at Barrow. The solid line indicates 1:1 ratio of LWP and IWP.

Figure 9. Timeseries of liquid water path (LWP) and ice water path (IWP), for the median model values and ground-based retrievals. Retrieved LWP is calculated using the WANG method averaged between Barrow and Oliktok Point and the TURNER method averaged between Barrow, Oliktok Point, and Atqasuk. Retrieved IWP is calculated using the SHUPE-TURNER method at Barrow.

Figure 10. a) Time-averaged temperature from the models as a function of height. The properties depicted are a) the median of the models (solid line), the inner 50% (dotted line), and the min/max (dashed line); b) difference of the median value of the SCMs and CRMs from observations derived from ARM variational analysis. The averaging period is from 000 UTC Oct. 6 to 1400 UTC Oct. 8.

Figure 11. As in Figure 10, except for the water vapor mixing ratio.

Figure 12. Time-averaged modeled and observed downwelling surface LW flux as a function of a) the liquid water path (LWP), b) column cloud fraction. Time averaging is from 000 UTC Oct. 6 to 1400 UTC Oct. 8. Symbols plotted for each model indicate type (SCM versus CRM) and cloud microphysics scheme (one-moment with T-dependent partitioning "1-M, T-dep", one-moment with independent liquid and ice "1-M, Ind", and two-moment "2-M"). 'O' indicates observed values.

Figure 13. As in Figure 12, but for the downwelling surface SW flux.

Figure 14. Time-averaged liquid water path (LWP) from the sensitivity simulations with no ice microphysics as a function of the baseline simulated LWP. Time averaging is from 000 UTC Oct. 6 to 1400 UTC Oct. 8. Symbols plotted for each model indicate type (SCM versus CRM) and cloud microphysics scheme (one-moment with T-dependent partitioning "1-M, T-dep", one-moment with independent liquid and ice "1-M, Ind", and two-moment "2-M"). The solid line indicates 1:1 ratio of sensitivity to baseline LWP.

Figure 15. As in Figure 14, except for the sensitivity simulations with increased vertical resolution.

Figure 1. Map of the M-PACE analysis domain (region bounded by A1-A6) and location of the surface observing sites.

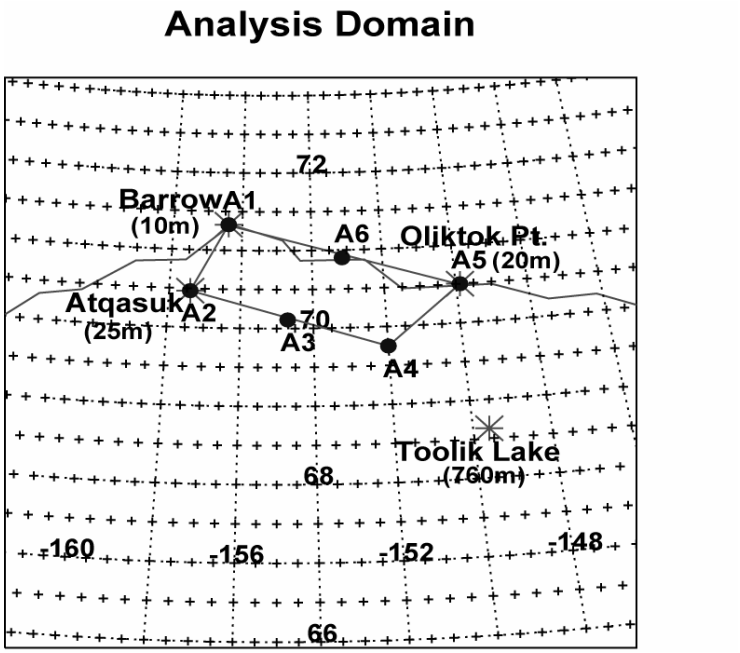

Figure 2. Time-height plot of the ARSCL-derived cloud fraction (%).

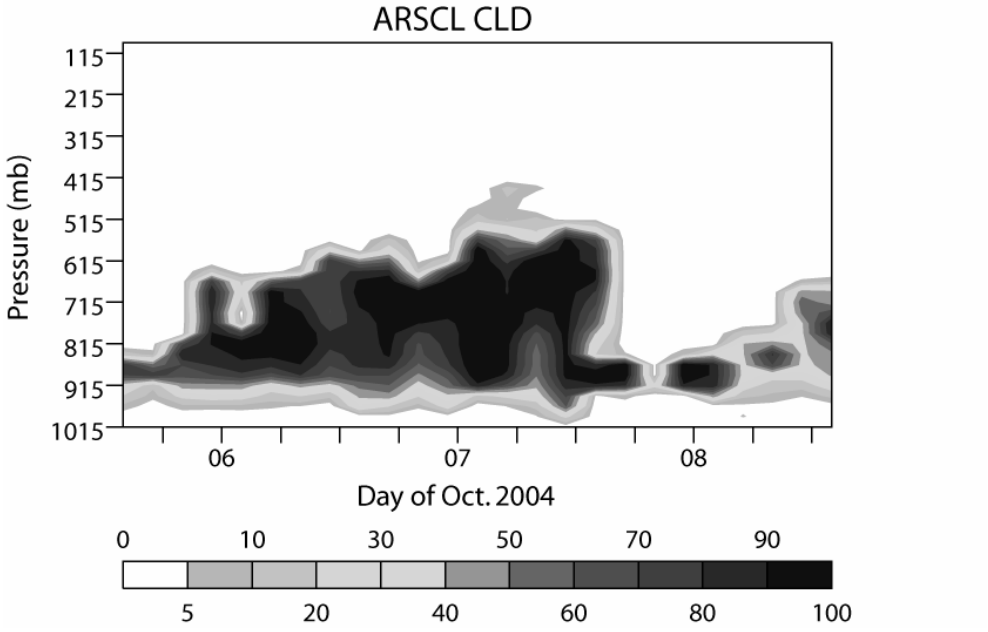

Figure 3. Example of an aircraft profile of liquid water potential temperature, θ_l (solid), liquid water content (dotted), ice water content (dash), observed during an ascent spiral at about 1917 UTC on Oct. 6.

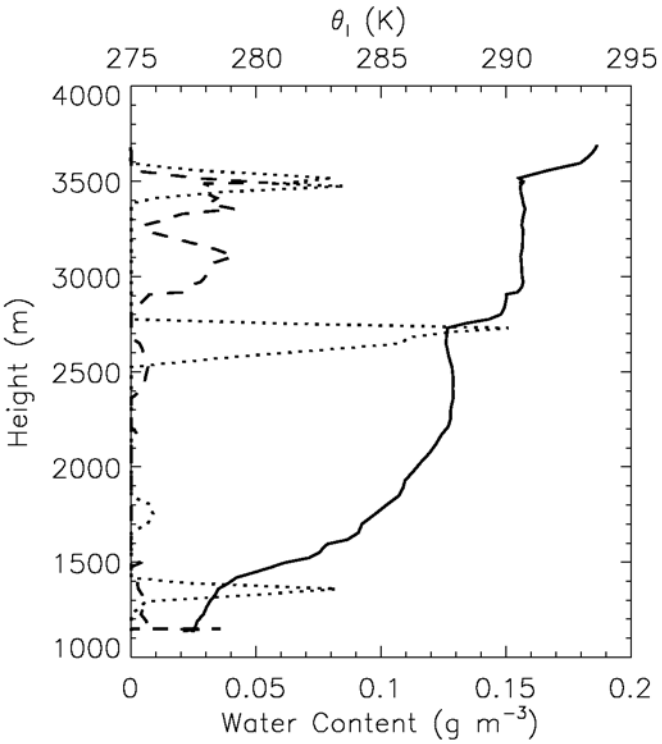

Figure 4. Time-height plot of the large-scale total advective tendencies of temperature and water vapor mixing ratio.

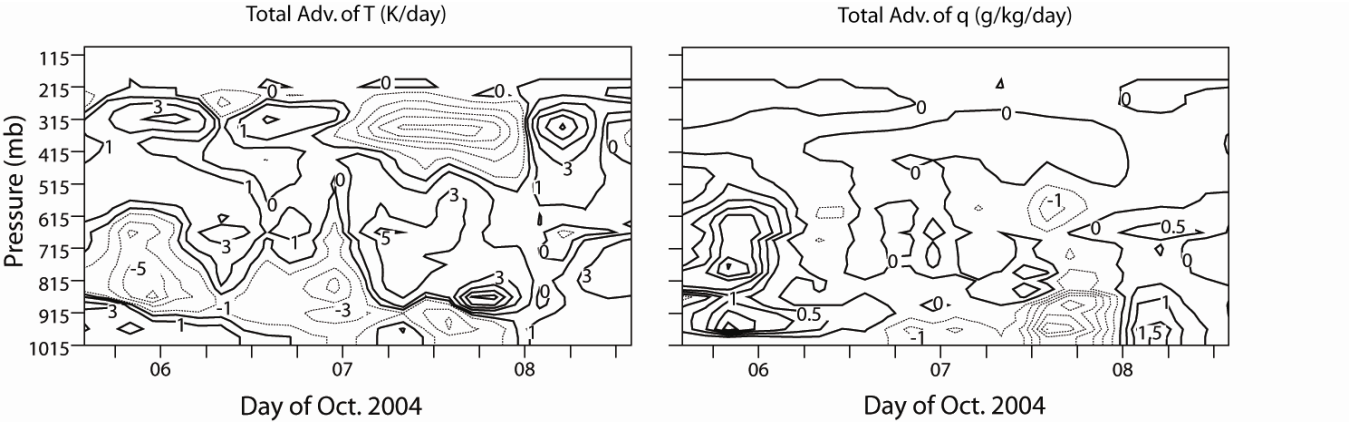

Figure 5. a) Time-averaged cloud fraction from observations and models as a function of height. The properties depicted are a) the median of the models (solid line), the inner 50% (dotted line), and the min/max (dashed line); b) the ARSCL observations (thick solid line with thin solid line indicated +/-1 st. dev.) and median of the SCMs and CRMs. The averaging period is from 000 UTC Oct. 6 to 1400 UTC Oct. 8.

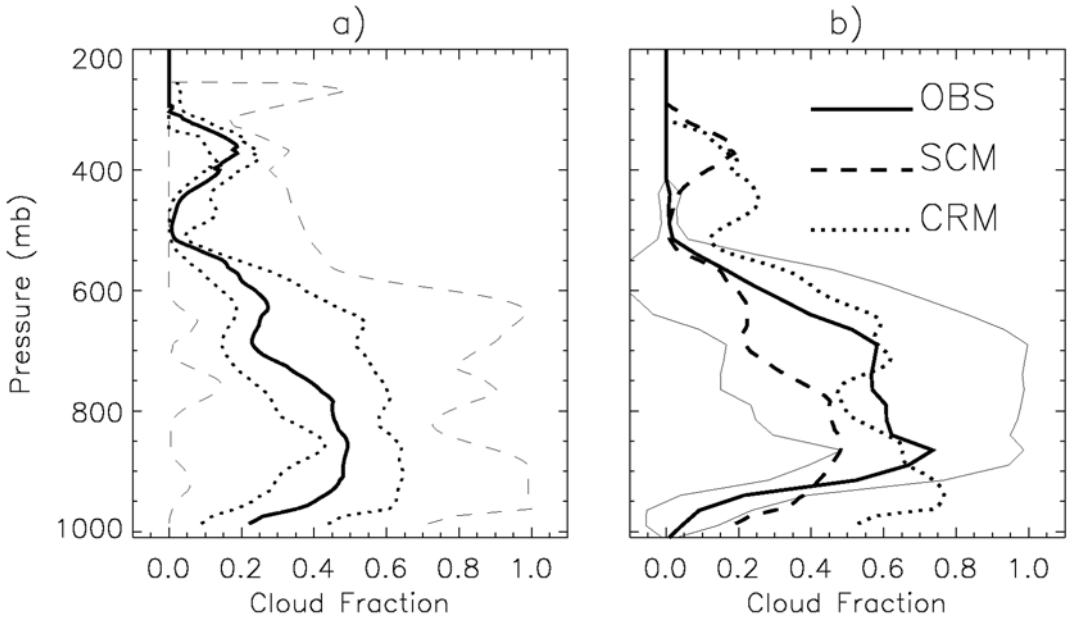

Figure 6. a) Time-averaged liquid water content from observations and models as a function of height. The properties depicted are a) the median of the models (solid line), the inner 50% (dotted line), and the min/max (dashed line); b) the aircraft observations (thick solid line with thin solid line indicating +/-1 st. dev.) and median of the SCMs and CRMs. The averaging period is from 000 UTC Oct. 6 to 1400 UTC Oct. 8 for the simulations. The aircraft value is the average of three flights that occurred on Oct. 5, 6, and 8.

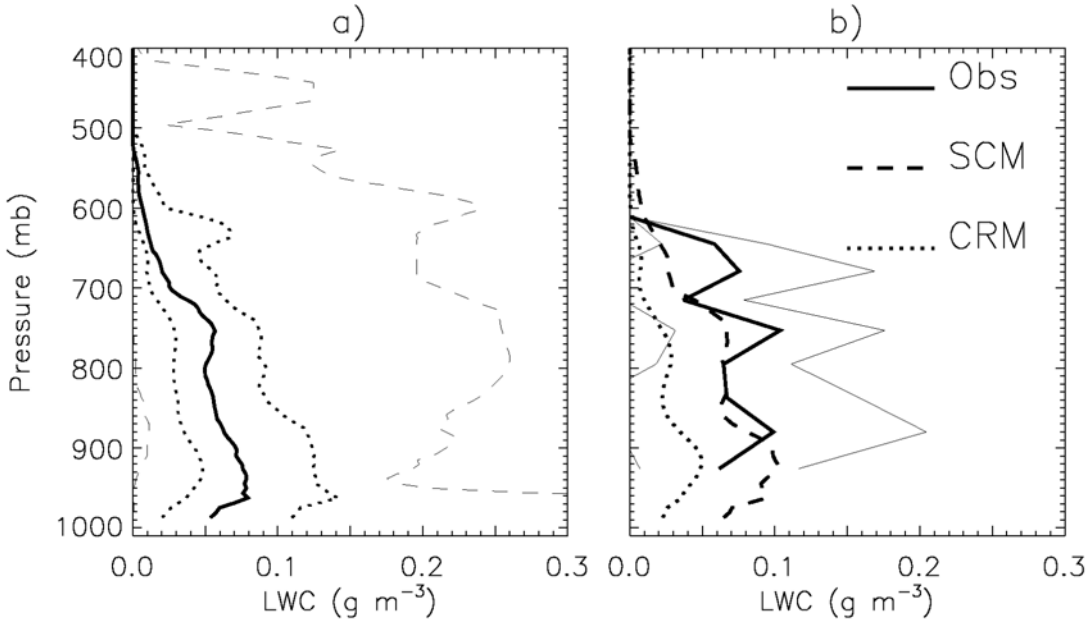

Figure 7. a) Time-averaged ice water content from observations and models as a function of height. The properties depicted are a) median of the models (solid line), the inner 50% (dotted line), and the min/max (dashed line); b) the aircraft observations 'AIR' (thick solid line with thin solid line indicating +/-1 st. dev.), SHUPE-TURNER radar retrievals 'RET' (thick dot-dash line with thin dot-dash line indicating +/-1 st. dev.), and median of the SCMs and CRMs. The averaging period is from 000 UTC Oct. 6 to 1400 UTC Oct. 8 for the simulations and radar retrievals. The aircraft value is the average of three flights that occurred on Oct. 5, 6, and 8.

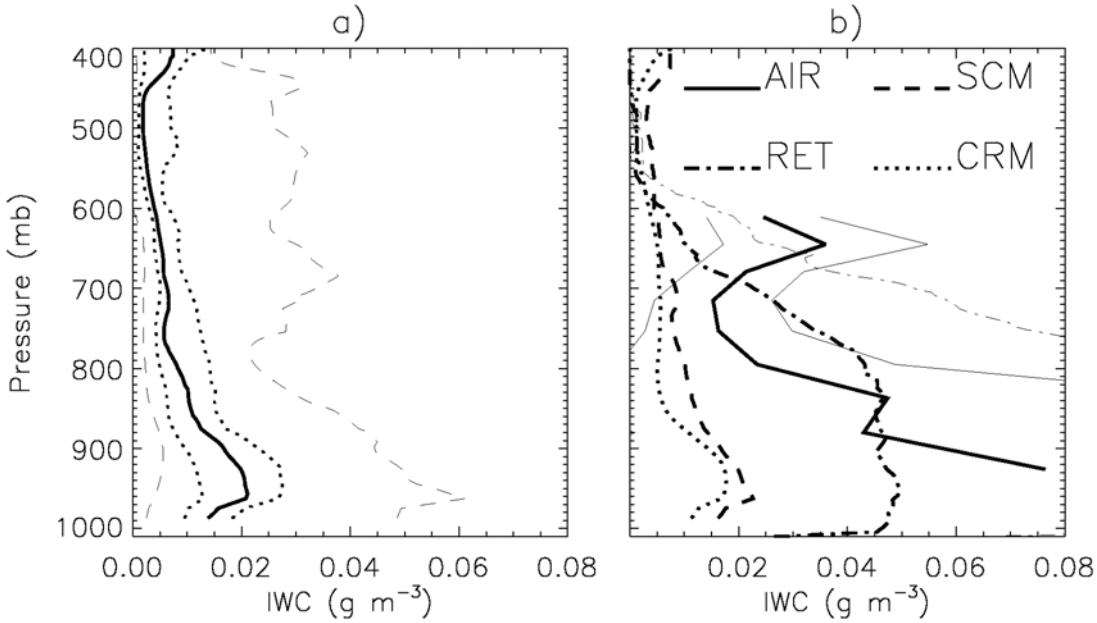

Figure 8. Time-averaged ice water path (IWP) as a function of liquid water path (LWP) for the models and ground-based retrievals. Symbols plotted for each model indicate type (SCM versus CRM) and cloud microphysics scheme (one-moment with T-dependent partitioning "1-M, T-dep", one-moment with independent liquid and ice "1-M, Ind", and two-moment "2-M"). "Cloud ice only" indicates the models that did not report precipitation ice. "T" and "W" indicate LWP retrievals using the TURNER method averaged between Barrow, Oliktok, and Atqasuk, and WANG method averaged between Barrow and Oliktok, respectively, and retrieved IWP using the SHUPE-TURNER method at Barrow. The solid line indicates 1:1 ratio of LWP and IWP.

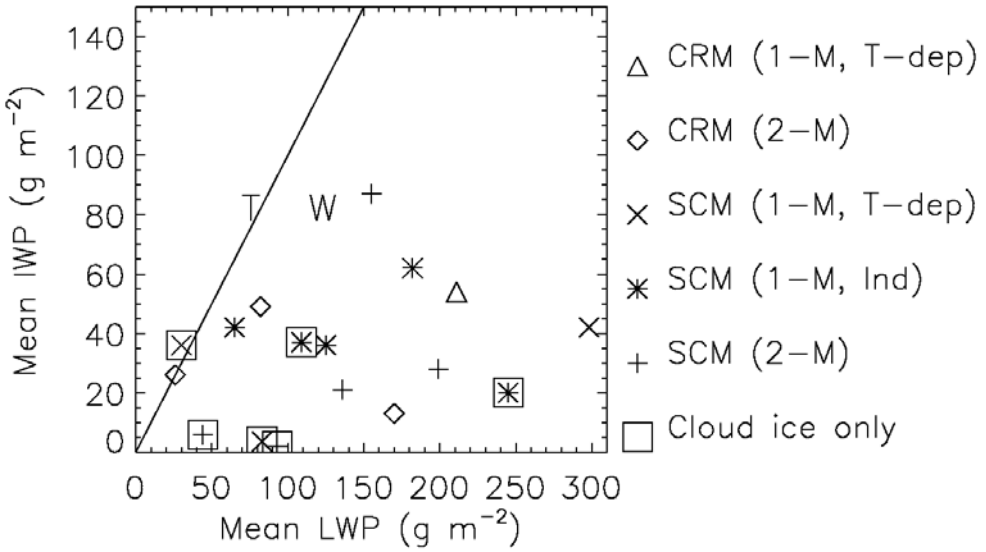

Figure 9. Timeseries of liquid water path (LWP) and ice water path (IWP), for the median model values and ground-based retrievals. Retrieved LWP is calculated using the WANG method averaged between Barrow and Oliktok Point and the TURNER method averaged between Barrow, Oliktok Point, and Atqasuk. Retrieved IWP is calculated using the SHUPE-TURNER method at Barrow.

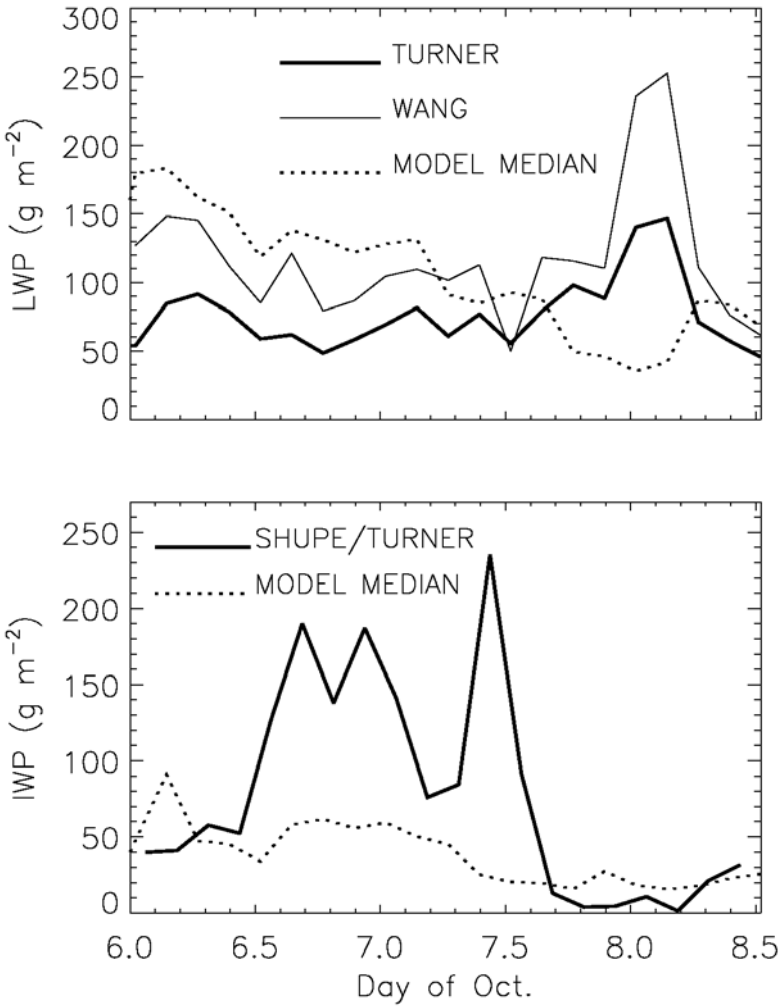

Figure 10. a) Time-averaged temperature from the models as a function of height. The properties depicted are a) the median of the models (solid line), the inner 50% (dotted line), and the min/max (dashed line); b) difference of the median value of the SCMs and CRMs from observations derived from ARM variational analysis. The averaging period is from 000 UTC Oct. 6 to 1400 UTC Oct. 8.

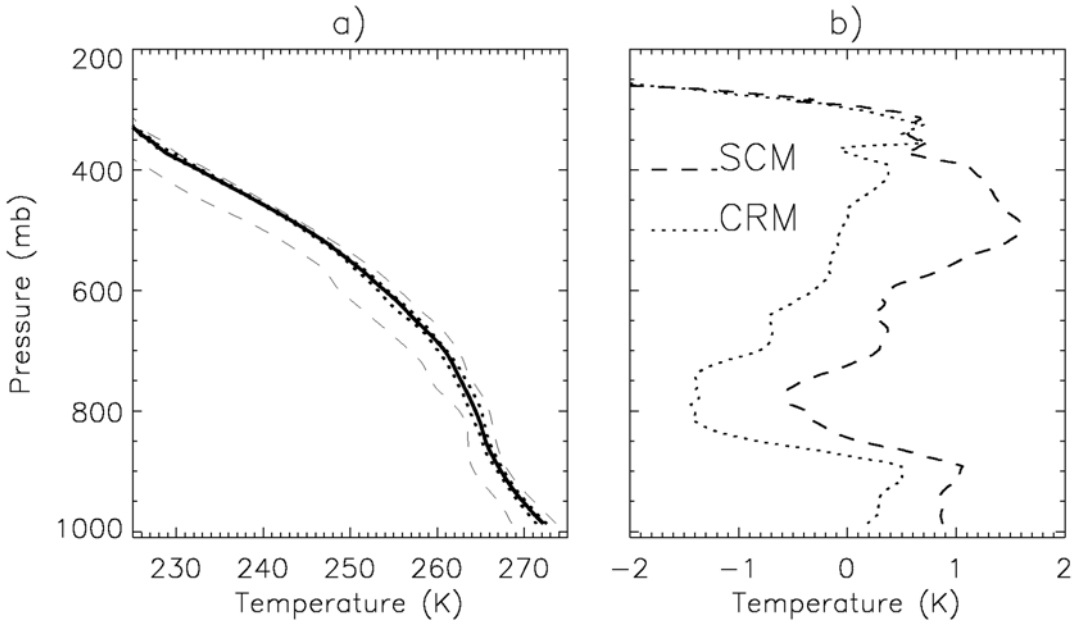

Figure 11. As in Figure 10, except for the water vapor mixing ratio.

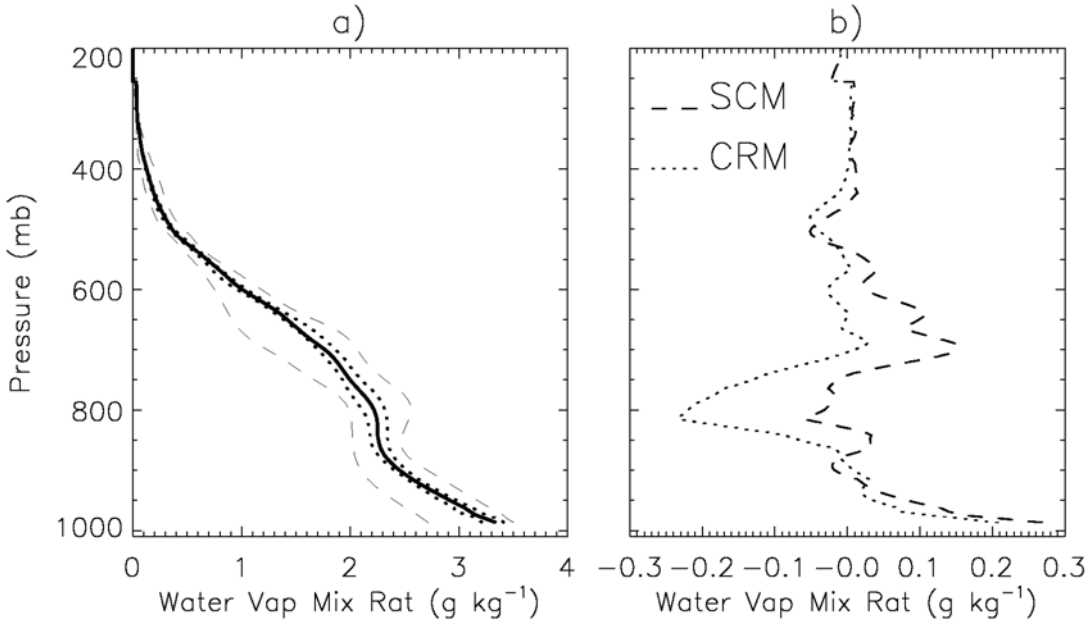

Figure 12. Time-averaged modeled and observed downwelling surface LW flux as a function of a) the liquid water path (LWP), b) column cloud fraction. Time averaging is from 000 UTC Oct. 6 to 1400 UTC Oct. 8. Symbols plotted for each model indicate type (SCM versus CRM) and cloud microphysics scheme (one-moment with T-dependent partitioning "1-M, T-dep", one-moment with independent liquid and ice "1-M, Ind", and two-moment "2-M"). 'O' indicates observed values.

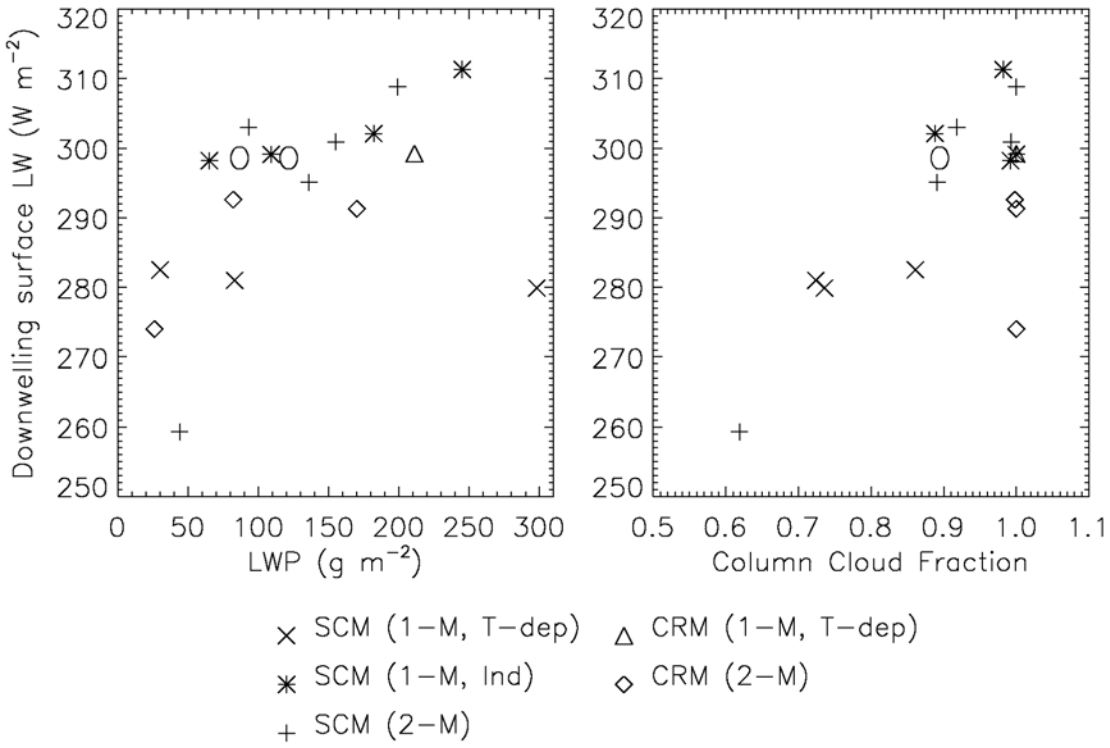

Figure 13. As in Figure 12, but for the downwelling surface SW flux.

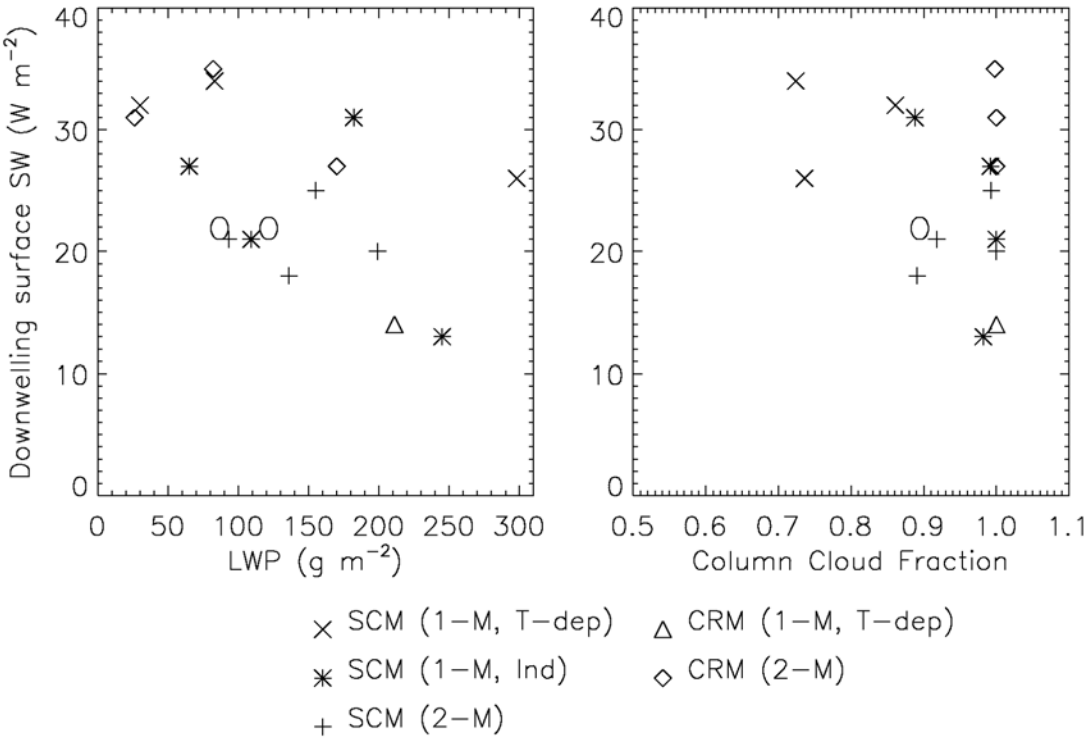

Figure 14. Time-averaged liquid water path (LWP) from the sensitivity simulations with no ice microphysics as a function of the baseline simulated LWP. Time averaging is from 000 UTC Oct. 6 to 1400 UTC Oct. 8. Symbols plotted for each model indicate type (SCM versus CRM) and cloud microphysics scheme (one-moment with T-dependent partitioning "1-M, T-dep", one-moment with independent liquid and ice "1-M, Ind", and two-moment "2-M"). The solid line indicates 1:1 ratio of sensitivity to baseline LWP.

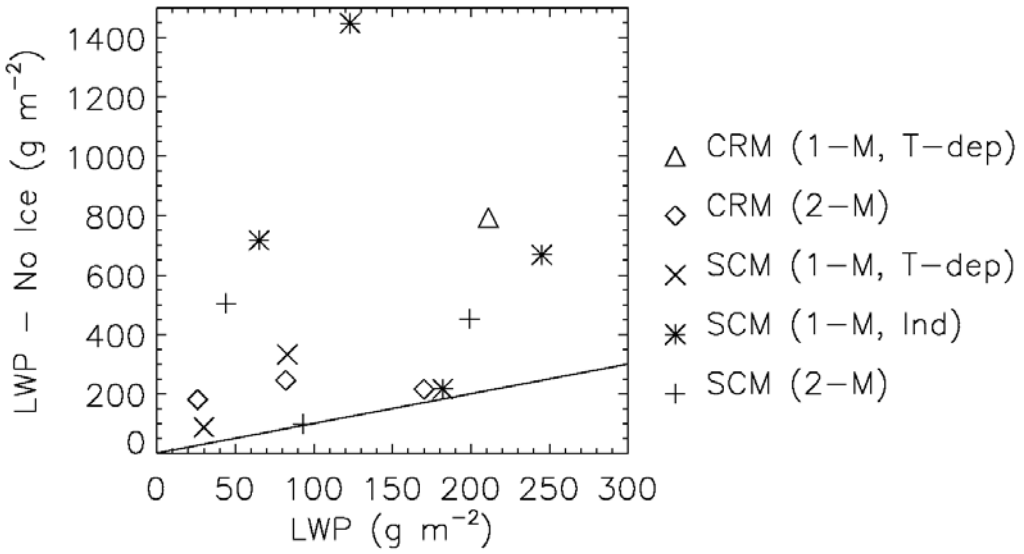

Figure 15. As in Figure 14, except for the sensitivity simulations with increased vertical resolution.